Scatter Correction Using a Primary Modulator on a Clinical Angiography C-arm CT System

Bastian Bier,* Martin Berger,† and Andreas Maier

Pattern Recognition Lab, Friedrich-Alexander-University Erlangen-Nuremberg, Erlangen, Germany

Marc Kachelrieß

Medical Physics in Radiology, German Cancer Research Center (DKFZ), Heidelberg, Germany

Ludwig Ritschl

Siemens Healthcare GmbH, Forchheim, Germany

Kerstin Müller, Jang-Hwan Choi, and Rebecca Fahrig

Radiological Sciences Lab, Stanford University, Stanford, CA, USA

(Dated: January 5, 2017)

Abstract

Purpose: Cone-beam computed tomography (CBCT) suffers from a large amount of scatter, resulting in severe scatter artifacts in the reconstructions. Recently, a new scatter correction approach, called improved primary modulator scatter estimation (iPMSE), was introduced. That approach utilizes a primary modulator that is inserted between the X-ray source and the object. This modulation enables estimation of the scatter in the projection domain by optimizing an objective function with respect to the scatter estimate. Up to now the approach has not been implemented on a clinical angiography C-arm CT system.

Methods: In our work, the iPMSE method is transferred to a clinical C-arm CBCT. Additional processing steps are added in order to compensate for the C-arm scanner motion and the automatic X-ray tube current modulation. These challenges were overcome by establishing a reference modulator database and a block matching algorithm. Experiments with phantom and experimental in vivo data were performed to evaluate the method.

Results: We show that scatter correction using primary modulation is possible on a clinical C-arm CBCT. Scatter artifacts in the reconstructions are reduced with the newly extended method. Compared to a scan with a narrow collimation, our approach showed superior results with an improvement of the contrast and the contrast-to-noise ratio for the phantom experiments. In vivo data are evaluated by comparing the results with a scan with a narrow collimation and with a constant scatter correction approach.

Conclusion: Scatter correction using primary modulation is possible on a clinical CBCT by compensating for the scanner motion and the tube current modulation. Scatter artifacts could be reduced in the reconstructions of phantom scans and in experimental in vivo data.

* Also with the Graduate School 1773 "Heterogeneous Image Systems", Erlangen, Germany.; bastian.bier@fau.de

† Also with the Graduate School 1773 "Heterogeneous Image Systems", Erlangen, Germany.

I. INTRODUCTION

Scattered radiation is one of the major problems in cone-beam computed tomography (CBCT) that affects image quality and quantitative CBCT imaging. A large amount of scatter is measured due to the large irradiated volume and the large area detector, resulting in a high scatter-to-primary ratio (SPR) in the measured signal [1]. Ignoring the scatter during the reconstruction results in severe scatter artifacts such as cupping artifacts, shadow artifacts, and contrast loss in the reconstructed images [2].

Different approaches exist in the literature to reduce scatter artifacts. In general, these methods can be divided into two groups: scatter rejection and scatter correction methods [2]. The first mentioned, hardware-based, group makes modifications in the imaging geometry with the objective to reduce the measured scatter that reaches the detector. The most widely used method is the insertion of an antiscatter grid (ASG) [3, 4], which reduces the amount of measured scatter. However, depending on the design of the antiscatter grid, also parts of the primary radiation get attenuated. Hsieh et al. [5] proposed a modified antiscatter gird, called striped ratio anti grid, which enables both reduction and estimation of scatter in the projection images. Further geometric considerations to reduce scatter are the air gap [6], which describes the distance of the object to the source, or collimation [7], which limits the field-of-view (FOV).

The second group consists of software-based scatter correction methods, which have two steps: a scatter estimation and a scatter compensation step [8]. These methods estimate the scatter in the projection or image domain. Measurement-based method use measured scatter signal [9], a beam-stopper array [10], or static or moving beam blockers [11–13]. To the model-based scatter estimation belong beam-scatter-kernel methods [14, 15] or models based on Monte Carlo approaches [16–19], which are based on the physics of the X-ray path through the scanned object. The estimation and compensation are often intertwined in an iterative manner. In order to achieve a clinically satisfying image quality, hardware and software-based methods are combined in current clinical C-arm CT systems.

Another measurement-based scatter estimation approach uses a primary modulator, which is placed in between the X-ray source and the object, see Figure 1 [20, 21]. The primary modulator is a pattern, consisting of transparent and semitransparent blocks, such that parts of the primary radiation get modulated with a high-frequency pattern. The

assumption is that primary radiation does not result in high frequency scatter components and that scatter is a pure low frequency signal [21]. This enables separation of the primary from the secondary radiation in the measured signal. In a first attempt, Zhu et al. applied filtering in the Fourier domain of the projection images in order to separate both signals [21] and improved this method recently [22]. The characteristics of the modulator pattern (thickness, block size, material) have been optimized to achieve a good scatter estimate by simultaneously reducing the introduced beam-hardening effects [23–28]. Further, Grimmer et al. presented a method able to remove the introduced beam hardening [29]. They calculate coefficients from a calibration scan to correct the acquired data for non-linearities. Another approach presented by Schorner et al. adds temporal modulation, which improves the reconstruction of high-frequency information of the objects [30]. However, these approaches have in common that they rely on a perfect homogeneous modulator pattern, which is hard to manufacture. Further, temporal X-ray tube current modulation is complex to implement on a clinical system. Recently, Horváth et al. compared different primary modulator scatter correction methods [31]. One of these methods is an approach of Ritschl et al. They proposed a new method called improved Primary Modulator Scatter Estimation (iPMSE), which is robust to inaccuracies in the modulation pattern [32]. Instead of filtering the projection images in the Fourier domain, an objective function is solved patch-wise in projection space, showing promising results on a table top CBCT system.

The aim of this work is to transfer the iPMSE method of Ritschl et al. [32] to a clinical C-arm CBCT system, where the imaging geometry is changing between individual projection images. First results of this method were presented recently [33]. Challenges arise due to the C-arm motion when the C-arm is rotating and the tube current modulation of such systems, influencing the projected modulator pattern in terms of amplitude and location. A method is proposed, which can compensate for the C-arm motion and the tube current modulation. The new proposed algorithm is named *C-arm iPMSE* and is tested on phantom and on experimental in vivo data.

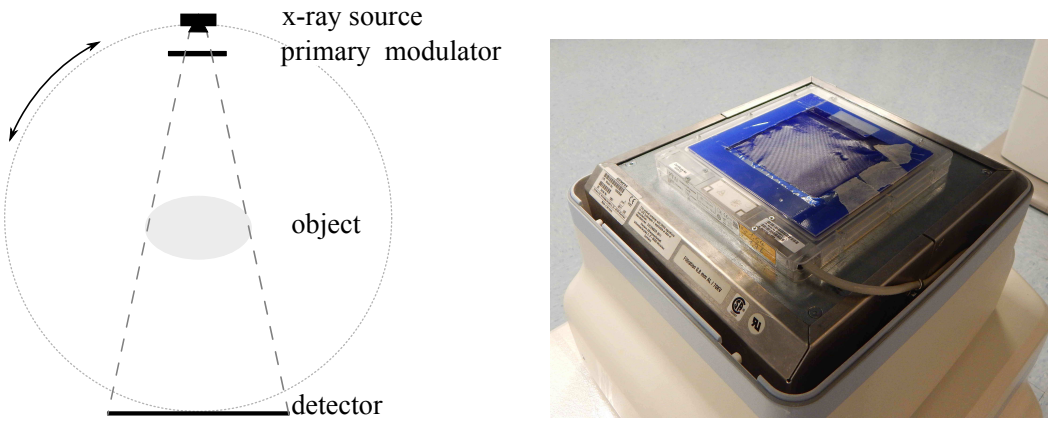

(a) (b)

FIG. 1. Imaging geometry of the C-arm CBCT system with a primary modulator, shown in Figure 1(a). Figure 1(b) shows the erbium primary modulator mounted on the collimator housing of a C-arm, in front of the X-ray source.

II. MATERIALS AND METHODS

A. Theory

1. *The primary modulator*

The used primary modulator in this work consists of erbium with a block size of 0.457 mm and a thickness of 0.0252 mm, which is the same as used in reference [32]. The transmission of the semitransparent blocks is 80.5% at 120 kV [27]. Erbium has been proved to reduce the beam hardening effect, introduced by the additional material of the modulator [28].

2. *The improved Primary Modulator Scatter Estimation (iPMSE)*

The iPMSE scatter correction algorithm of Ritschl et al. is briefly explained in the following paragraph to outline the challenges to transfer the algorithm to a clinical C-arm CT system [32]. In order to estimate the scatter, the algorithm requires two projection images: a projection of the modulator only, called reference modulator image $\boldsymbol{m}$, and a projection with the modulator and the object in place, called $\boldsymbol{c_m}$ in the following. Two example projections $\boldsymbol{m}$ and $\boldsymbol{c_m}$ are shown in Figure 2(a) and Figure 2(b), respectively. $\boldsymbol{m}$ can be acquired in a calibration scan before or after the object scan. Having both projection

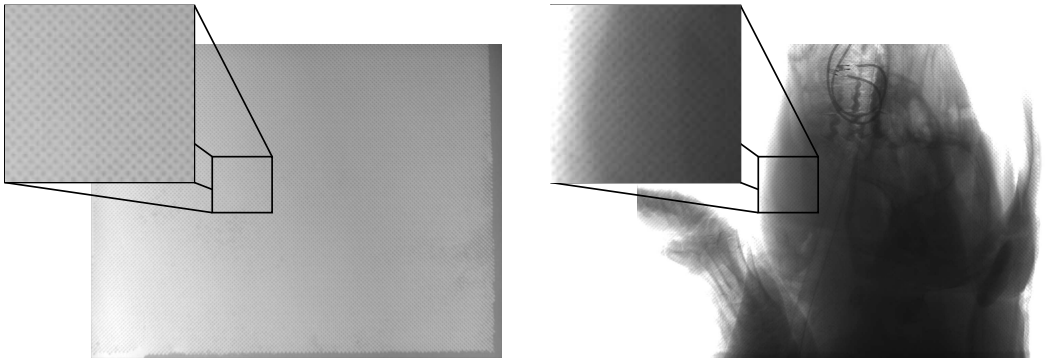

(a) Projection image of the primary modulator $\boldsymbol{m}$.

(b) Projection image of the modulator and the object $\boldsymbol{c_m}$.

FIG. 2. Projections required as input for the iPMSE algorithm.

images available, the algorithm minimizes the following objective function C:

$$C(\boldsymbol{c}_p^{est}) = ||\boldsymbol{D} \cdot \boldsymbol{M}^{-1} \cdot (\boldsymbol{c}_m - \boldsymbol{c}_s^{est})||_1 \quad \text{, where} \tag{1}$$

$\boldsymbol{D}$ is a matrix, which describes the spatial gradient and $\boldsymbol{M}$ is a diagonal matrix containing the measured transmission of the measured projection $\boldsymbol{m}$, which does only contain the attenuation of the modulator. Note that the measured values in m are normalized by I_0, which is the energy of the unattenuated X-ray. The vectors $\boldsymbol{c_s}^{est}$ and $\boldsymbol{c_m}$ describe the estimated scatter and the measured projection image, respectively. The equation states that if the scatter is estimated correctly, the modulator disappears in the projection image and thus the gradient is minimal. It is further assumed that the scatter consists of low frequencies only. This is assured by solving Equation 1 patch wise. The patches do not overlap and their size should be large enough to cover a full period of the modulator pattern [32]. For each of these patches, a constant scatter estimate is calculated, yielding in a low frequency scatter estimate. The solution for each patch is found with a line search algorithm. In order to obtain the final scatter estimate, $\boldsymbol{c_s}^{est}$ is additionally filtered with a mean and a median filter. The corrected projection image $\boldsymbol{c_p}^{est}$ is then estimated by subtracting the scatter estimate and multiplication with the inverse modulator pattern: $\boldsymbol{c_p}^{est} = \boldsymbol{M}^{-1} * (\boldsymbol{c_m} - \boldsymbol{c_s}^{est})$.

Note that the inverse modulator pattern $\boldsymbol{M}^{-1}$ is multiplied with the measured images $\boldsymbol{c_m}$ in the optimization formula and in the estimation for the scatter corrected projection. Thus, it is essential that the projected modulator pattern in both images $\boldsymbol{m}$ and $\boldsymbol{c_m}$ are identical in terms of their location and amplitude. Deviations could result in incorrect scatter

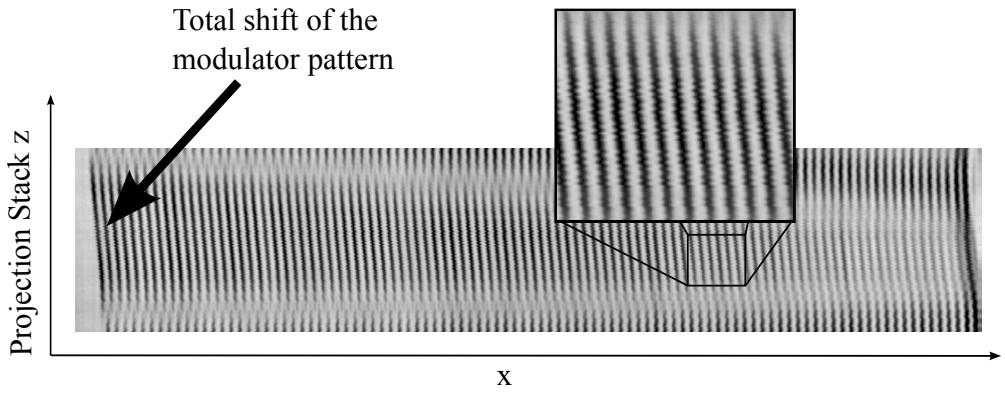

FIG. 3. Reordered projection image stack. The motion and the resulting deformation is visible in the projected lines of the modulator pattern.

estimates and in residual modulator pattern, visible in the corrected projection images. The changing imaging geometry and the tube current modulation of C-arm CBCT systems lead to violations of these conditions.

3. Influence of C-arm motion

During a 3D rotational acquisition, the C-arm rotates 200° around the object. Due to gravital force on the C-arm, where the X-ray tube and flat detector are mounted, the modulator pattern changes its position on the detector. The deformation results in a shift of the modulator pattern on the detector of up to 15 pixels from the first to the last acquired projection image. This shift can be seen in a reordered projection image stack of a modulator pattern acquisition, shown in Figure 3. The arrow indicates, how the border of the projected pattern shifts during the rotation. The wobbling of the C-arm causes the modulator pattern to be in a slightly different position in adjacent projections. This results in the jagged projection lines shown in the zoomed region in Figure 3. On a table top system, these lines would be perfectly vertical.

4. Influence of the automatic exposure control

Clinical C-arm CT systems adjust the exposure parameter (tube current, exposure time, and tube voltage) to achieve a preset detector entrance dose dependent on the current object.

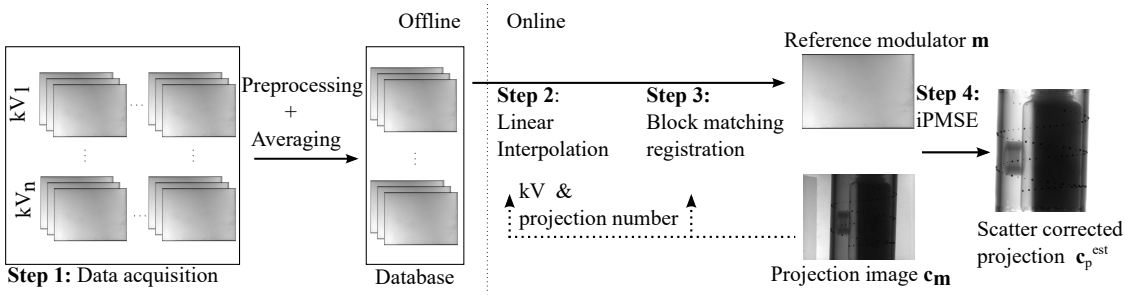

FIG. 4. Pipeline of the proposed *C-arm iPMSE* method.

If a primary modulator is mounted on the X-ray source, the X-rays get attenuated in the semitransparent parts of the modulator. Due to the changing voltage, the projected modulator amplitude changes due to the energy-dependent attenuation of the modulator material. This leads to a different projected modulator amplitude from projection to projection as the applied voltage changes. This lead to inaccuracies in the scatter estimation.

B. C-arm iPMSE

The schematic outline of the proposed iPMSE algorithm for C-arm CT systems is given in Figure 4. The first step of the *C-arm iPMSE* algorithm is to establish a reference modulator database containing projection images of the modulator only, acquired at different tube voltages and angles. For each voltage and angle, three images are acquired and averaged in order to reduce noise in the pattern. This is done in an offline calibration step before the actual object acquisition. The database contains images in intensity domain. During scatter correction, the database is used to create a reference modulator pattern. Currently, a linear interpolation method is implemented to generate the appropriate reference modulator pattern during a 3D rotational scan. This step solves two problems: first, the positions of the pattern are roughly aligned, since they are acquired at the same angular position of the C-arm. Second, the correct amplitude of the modulator projection in the projection $\boldsymbol{c_m}$ is estimated sufficiently for the iPMSE algorithm. It needs to be mentioned that the interpolation method may vary for different modulator materials.

After the rough alignment of the pattern, the projected pattern in the projections $\boldsymbol{m}$ and $\boldsymbol{c_m}$ has to be refined in a subpixel range. It is assumed that only rigid motion of the modulator pattern can occur. The translational component is due to the C-arm motion. A rotation can occur if the X-ray source or the detector slightly rotate, or due to the non

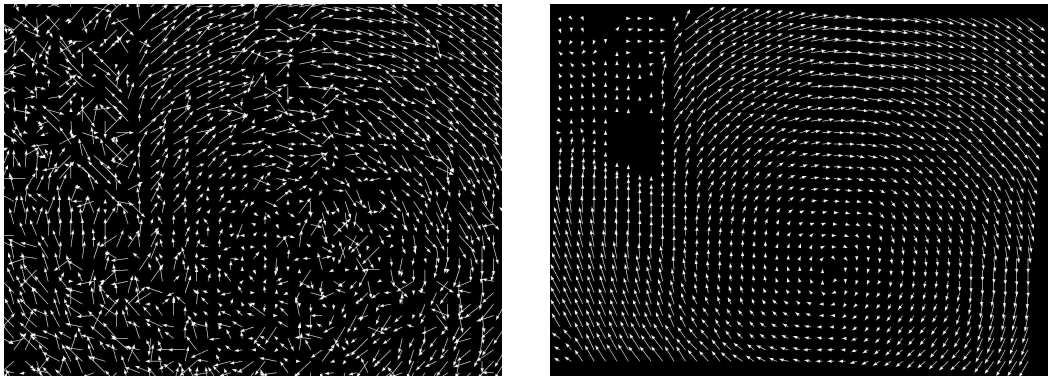

(a) (b)

FIG. 5. (a) Initial 2D motion vector field after block matching registration. (b) 10 x 10 pixel median filtered final 2D motion vector field.

stiffness of the modulator attached to the X-ray source. Additionally, the visibility of the modulator pattern is impaired behind dense objects, which makes the alignment task more challenging (cf. Figure 2(b)). The modulator alignment is estimated by a block matching registration [34]. This method subdivides the images into blocks and calculates a blockwise translation, by maximization of the correlation coefficient. The block size is set to 13 pixels and the sub-pixel accuracy to 0.1 pixels. An example 2D vector motion field is shown in Figure 5(a). The initial motion field is filtered by a 10 x 10 median filter, resulting in the filtered motion field as shown in Figure 5(b). Note, that the arrows are scaled up to permit visualization and the actual estimated translation at the border of the projection measured to be 1.5 pixels maximum. In a first order approximation rotation is negligible and a pure translation of the filtered motion field for each patch in the scatter correction process estimates the correct position sufficiently well. Grimmer et al. used a similar registration step, which was necessary to compensate for instabilities of the focal spot [29]. In contrast to our approach, they computed a single 2D translation for each projection to correct for this effect.

C. Data Processing

The data processing and 3D reconstruction is implemented in CONRAD, an open-source software for simulation and reconstruction for cone-beam data [35]. The measured intensity on the detector is preprocessed and normalized with the energy of the unattenuated X-ray

beam I_0 [36]. For that, flat-field acquisitions with known mAs were acquired. Note that the mAs has no influence on the modulator amplitude, after the measured raw value is converted to the intensity domain. Then, the proposed *C-arm iPMSE* scatter correction algorithm is applied with a patch size of 13×13 pixels. Afterwards, the negative logarithm and a noise suppression as suggested by Zhu et al. is performed [1]. In their approach, the noise statistics are modeled in the scatter corrected projection images and a penalized weighted least-squares algorithm with an edge-preserving regularization is used to estimate the noise. A noise suppression after scatter correction is crucial, since noise increases tremendously in scatter corrected images [2, 21, 37]. This is because only the low frequency scatter part is subtracted from the measured signal, leaving the high frequency noise untouched. Without a suitable noise suppression, the benefits of a scatter correction are superimposed by increased noise statistics. The smoothing parameter β of this noise suppression algorithm is selected, such that the modulation transfer function (MTF) of the reconstruction results is similar. Afterwards, a truncation correction and the standard FDK reconstruction algorithm [38] with a Shepp Logan kernel is performed. In a last step, a ring artifact correction is applied to the reconstructions [39].

D. Data Acquisition

All datasets were acquired with a Siemens Artis zeego C-arm system (Siemens Healthcare GmbH, Forchheim, Germany). The focal spot size was set to 0.3 mm in order to minimize the penumbra effect. Over 200°, 248 projection images with a size of 1240×960 pixels were acquired. The pixel size is isotropic 0.308 mm. In this study, a prototype software application enables manual control of the tube output on the C-arm CT system. This software enables to built up the database with reference modulator patterns acquired at 50, 70, 90, 100, 109, and 120 kV.

For all experiments, we conducted three scans: first, a scan with full FOV; second, a scan with a narrow collimation, where the z-collimator aperture, i.e. the field of view in z-direction, was minimal in order to reduce the irradiated volume; and third, an acquisition with the modulator mounted. The size of the collimation is approximately 20 mm in the isocenter. A smaller collimation or slit scan is not possible with the used system.

The phantom experiment was performed with the Electron Density Phantom (model

(a) Phantom containing the complete Electron Density Phantom.

(b) Phantom containing the inner ring of the Electron Density Phantom.

FIG. 6. Electron Density Phantom used for the phantom experiments.

M062, CIRS, Norfolk, VA, USA). The inner disk of the electron density phantom was filled with a liver, muscle, dense bone core, trabecular bone, dense bone, breast, lung exhale, and lung inhale insert (clockwise c.f. Figure 6). For the first experiment, the complete Electron Density Phantom was used. Additionally two large torso-shaped objects (27 cm lateral diameter) were placed next to the phantom to increase the amount of scatter and attenuation (c.f. Figure 6(a)). The tube voltage was constant at a maximum of 120 kV due to the high attenuation of the large phantom. This experiment was performed with and without an antiscatter grid. For the next experiment, only the inner disk of the Electron Density Phantom was scanned with an additional water bottle and additional material plugs placed next to the phantom (c.f. Figure 6(b)). These additional objects have been placed there only for the modulator acquisition causing the tube voltage to vary between 90 and 120 kV during the acquisition.

The protocol for this in vivo animal study was approved by Stanford Universitys Administrative Panel on Laboratory Animal Care. One Yorkshire pig (approximately 50 kg) was used for this study. Arterial femoral access was established using percutaneous puncture for hemodynamic monitoring.

TABLE I. Smoothing parameter β used for the reconstructions.

	uniform scatter	*C-arm iPMSE*
Phantom big	0.001	0.0005
Phantom small	0.002	0.001
Pig head	0.002	0.001
Pig phantom	0.002	0.001

E. Evaluation Method

For each experiment, four reconstructions are calculated: an uncorrected reconstruction, a reconstruction of a narrow scan, a scatter corrected reconstruction using a constant scatter estimate [40], and a reconstruction using the proposed *C-arm iPMSE* method. The constant scatter correction method has a parameter C, which is set to 0.5. The same noise suppression algorithm is applied for both scatter corrected reconstructions. The used smoothing strength β for the different reconstructions are shown in Table I. As a quantitative measure, the contrast, the contrast-to-noise ratio (CNR), and the MTF is computed in the results of the phantom experiments. The CNR is computed using following formula:

$$CNR = \frac{|\mu_r - \mu_b|}{\sqrt{\frac{\sigma_r^2+\sigma_b^2}{2}}}, \tag{2}$$

, where μ_r and μ_b are the mean values of the ROI and their background, respectively. σ_r^2 and σ_b^2 are their corresponding variances. The ROIs and their background are indicated in Figure 13(a) with the blue and the orange ring, respectively. The contrast is the difference $|\mu_r - \mu_b|$. For the calculation of the MTF, the method proposed by [41] is used. In a circular region, line profiles are sampled over 360 degree vertically along a sharp circular edge as indicated in Figure 9(b). From these line profiles, a MTF curve is obtained. In the phantom experiments, ROI 5 is used for the MTF computation. We define a value in the MTF curve, where the MTF dropped to 50%, which is indicated with the dashed line in Figure 9(a). This value is called MTF50 in the following.

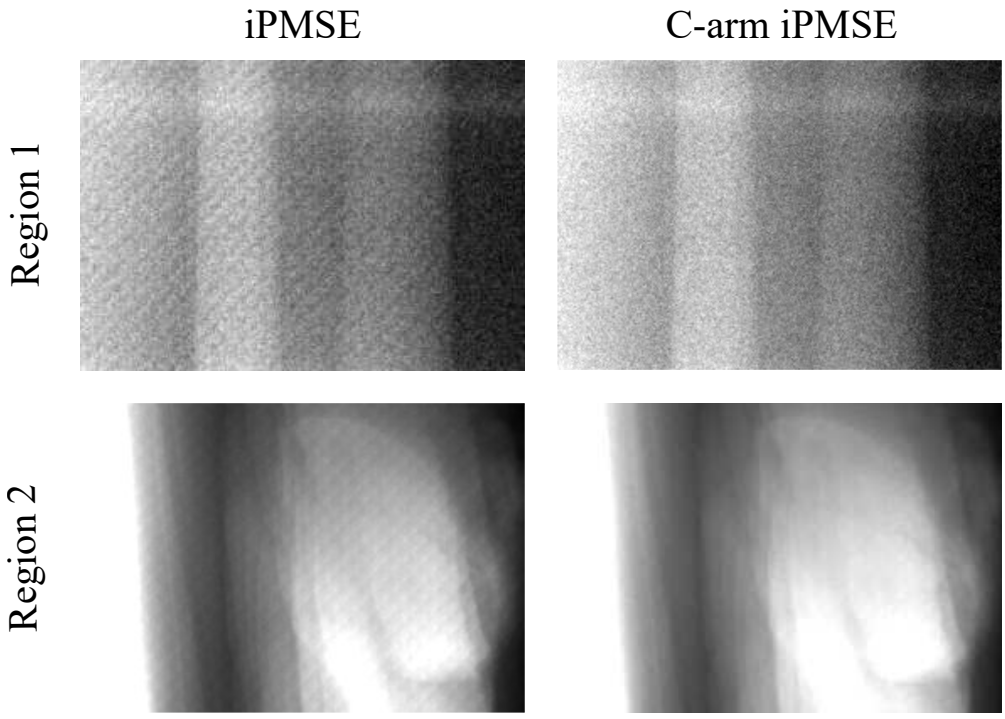

FIG. 7. Sub-regions of iPMSE and *C-arm iPMSE* corrected projection images. Phantom and in vivo data are shown in the top and bottom row, respectively.

III. RESULTS

In Figure 7, the result on projection images of the *C-arm iPMSE* method is shown. On the left, projection sub-regions are shown where the normal iPMSE algorithm is applied. Residual modulator can be seen in the projection images. With the additional steps of the *C-arm iPMSE* algorithm, the modulator pattern is removed. As mentioned in Section II A 2, a disappearing modulator pattern indicates a correct scatter estimate. Note that for the shown corrected projection image a reference modulator pattern has been used, which has been acquired at the same angular position. Thus, the deformation motion, which depends on the angular position and the different influence of the gravity on the source and the detector, is accounted for in this image. Therefore, the visible residual pattern results only from the uncompensated C-arm wobble motion. With the deformation motion, the visibility of the residual pattern would be severe.

In Figure 8, the effect of the applied noise suppression on projections and on a reconstruction is shown. In the reconstruction shown in Figure 8(d), a high amount of noise can be observed. In the bottom row, reconstructions with different smoothing parameter β

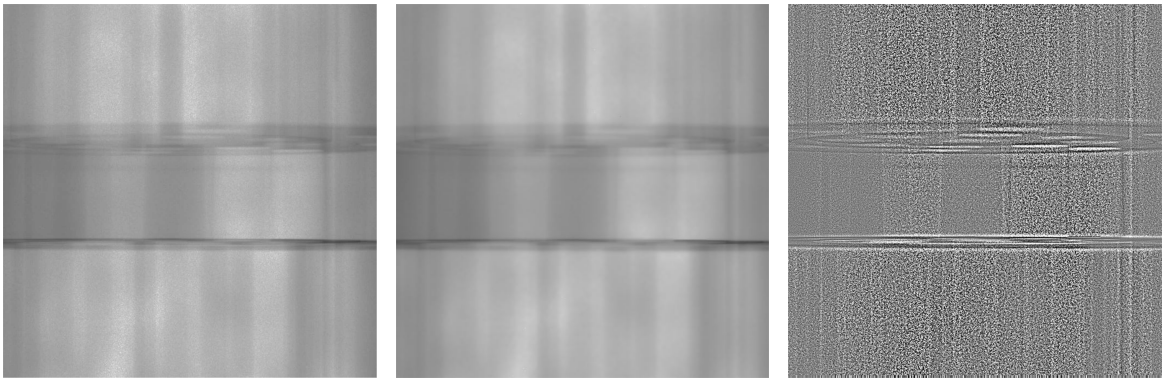

(a) Without noise suppression. (b) With noise suppression. (c) Difference image.

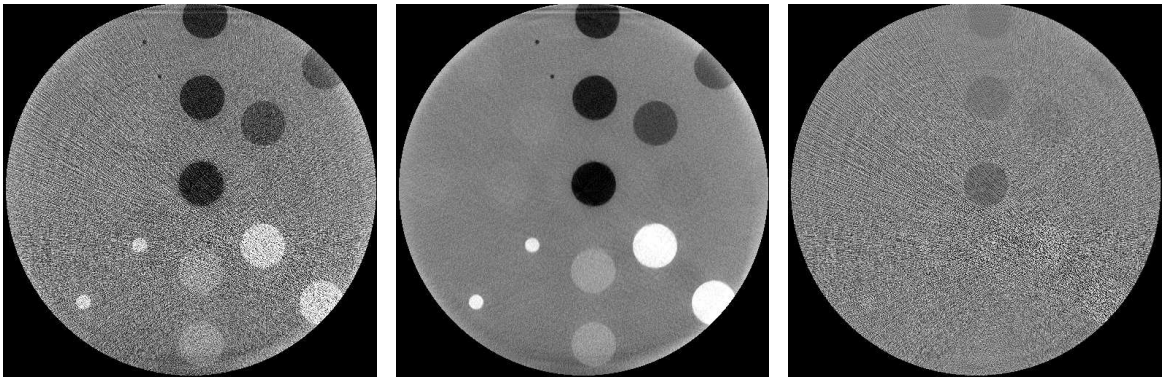

(d) Without noise suppression. (e) With noise suppression. (f) Difference image.

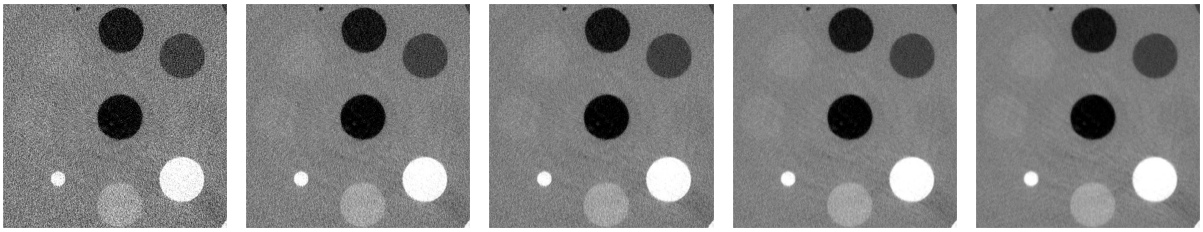

(g) $\beta = 0.0001$. (h) $\beta = 0.0003$. (i) $\beta = 0.0005$. (j) $\beta = 0.001$. (k) $\beta = 0.002$.

FIG. 8. Top row: projection images before and after noise suppression with their difference image. Center row: reconstructed images without and with noise suppression and their difference image. Bottom row: reconstructions using different smoothing parameters. Grayscale window for the reconstructions: $C = 0$ HU, $W = 2000$ HU.

are shown. A higher smoothing parameter β results in less noise and a higher contrast in the reconstructions, but also in a loss of sharpness. In order to quantify this trade off, the CNR values and the MTF50 value are calculated and shown in Table II. In Figure 9(a), the corresponding MTF curves are shown.

Center slices of the corrected and non-corrected reconstructions of the aforementioned

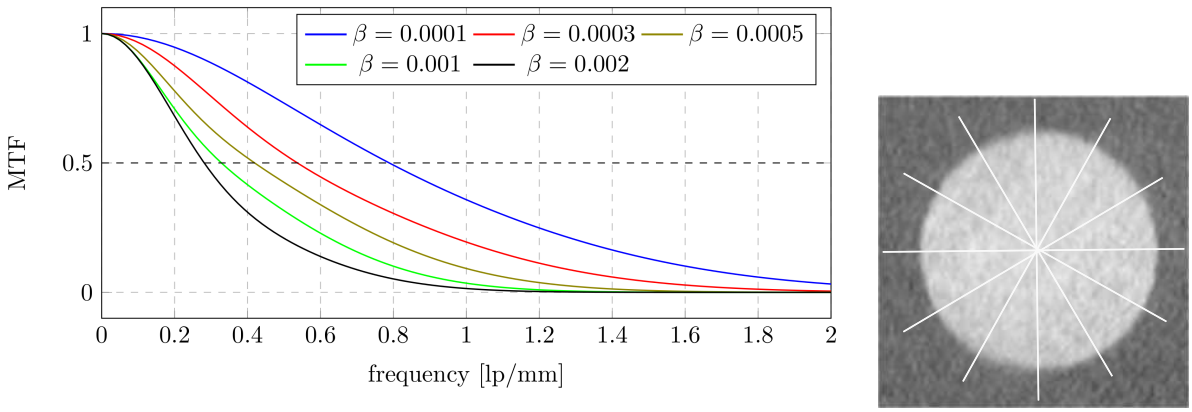

(a) (b)

FIG. 9. Left: MTF curves for different smoothing parameters β. Intersection of the dashed line with the MTF curve indicated the MTF50 value. Right: ROI 5 where the MTF was calculated in the reconstructions. Lines indicate the sampling for the MTF computation.

TABLE II. MTF50 value compared with the CNR for different smoothing parameters.

	$\beta = 0.0001$	$\beta = 0.0003$	$\beta = 0.0005$	$\beta = 0.001$	$\beta = 0.002$
CNR	2.57	4.37	5.93	8.31	11.48
MTF at 50%	0.79	0.53	0.42	0.33	0.28

phantom experiments are shown in Figure 11 and Figure 12. The first columns show the results of the full FOV scan without a scatter correction applied. In all three cases, scatter artifacts are distinctly visible; cupping and shadow artifacts as well as contrast loss are seen. The second columns show results of the scan with a narrow collimation, where the amount of scatter should be an order of magnitude lower compared to an uncollimated scan. The scatter artifacts are still present in these reconstructions, although, the cupping artifact was slightly suppressed, especially for the smaller phantom in Figure 12(b). The remaining presence of the cupping artifact in the narrow scan reconstructions can be explained by the too large opening of the narrow collimation as well as the large amount of scatter due to the large object size. The third column shows the results of the uniform scatter corrected images. In these reconstructions, the cupping artifact could be reduced, but the shadow artifacts remained. A dark ring is visible outside the FOV in these reconstructions. The last columns show reconstructions using the proposed *C-arm iPMSE* method. In all cases, the scatter

artifacts are mostly removed. A small cupping artifact was visible at the border region of the FOV, which may have also resulted from object truncation. In the reconstruction shown in Figure 12(d), some streaks and cupping at the very border are introduced. The streaks are due to additional highly absorbing objects placed next to the phantom.

Comparing the effect of the antiscatter grid in the scans of the full Electron Density Phantom, the biggest difference is visible for the full FOV scan, where the cupping artifact was slightly reduced. For the narrow scan and the *C-arm iPMSE* result, no noticeable differences can be observed visually.

The visual results are supported by line profiles through the shown axial slice, shown in Figure 13. In the line profiles of the non-corrected, the narrow scan , and the uniform scatter corrected reconstruction, the cupping artifact is noticeable by increasing values towards the boundary of the FOV. This artifact disappeared when using our proposed method. The contrast and the CNR in the reconstructions were computed for nine regions-of-interest (ROI) shown in Figure 13(a) and Figure 13(b). Table III shows that the averaged contrast and CNR values improve in the *C-arm iPMSE* scatter-corrected reconstructions as compared to the scatter-distorted and the narrow scan reconstructions. Further, the MTF50 was calculated in the reconstructed phantom images, which are shown in Table IV.

In Figure 10, we show two reconstruction results of the small phantom using a modulated and constant tube voltage (115 kVp). Qualitatively, no remarkable difference can be observed. The largest difference is the different presence of the overexposure artifact at the border of the object due to the different exposure settings. Note that for this acquisition a prototype software application has been used. Such a setting is not possible on a standard clinical scanner.

In Figure 14 and Figure 15, axial, sagittal, and coronal slices of the pig head and abdomen are shown. The first columns show uncorrected reconstructions of a full FOV scan, the second columns show reconstructions of the narrow scan, the third columns show reconstructions using the constant scatter correction, and the last columns show the new *C-arm iPMSE* corrected images. Similar scatter artifacts as with the phantom datasets can be observed. In the uncorrected images, cupping artifacts are introduced and the contrast of the bones is reduced. In the narrow scans, the cupping is reduced, especially for the head scan. This might be due to the relatively small irradiated volume in this case. In the results using the constant scatter correction, the scatter artifacts could be reduced slightly. Note that

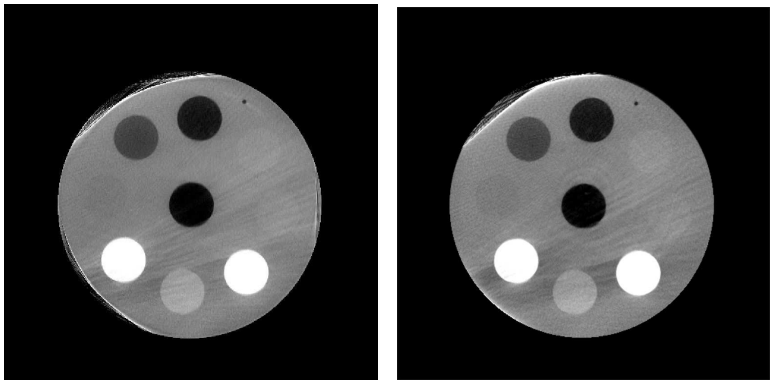

(a) With changing kVp. (b) With constant kVp.

FIG. 10. Reconstructions of the small phantom using a changing and constant tube voltage. Grayscale window for the reconstructions: $C = 0$ HU, $W = 2000$ HU.

TABLE III. Average contrast and CNR of the ROIs shown in Figure 13. (Contrast [HU] / CNR).

Experiment	Uncorrected	Narrow scan	Uniform Scatter	C-arm iPMSE
Big phantom with ASG	347.6 / 2.39	388.0 / 3.24	480.2 / 5.48	485.5 / 5.98
Big phantom without ASG	365.73 / 2.61	371.6 / 2.92	490.88 / 4.23	482.5 / 6.01
Small phantom with ASG	452.7 / 2.32	541.6 / 6.51	473.1 / 3.0	566.8 / 8.62

the smoothing parameter is higher than in the *C-arm iPMSE* corrected images, resulting in better low contrast visibility. In the *C-arm iPMSE* corrected image, these artifacts are mostly removed. In Figure 16, line profiles through the pig reconstructions are shown. The location and direction of the lines are indicated in the axial slices. The cupping is visible in the uncorrected and the narrow scan reconstruction, especially for the abdomen case. The contrast visibility in the bone is improved using *C-arm iPMSE*. Note, that the disappearing rip in Figure 15(h) is due to shifted table position in this scan due to the experimental setting.

IV. DISCUSSION

The evaluation of the new *C-arm iPMSE* method showed the potential of removing scattered radiation using a primary modulator in a clinical setting. Our new method was able to remove most of the scatter artifacts. In particular, the reduction of the cupping and the shadow artifacts overall improved the image quality. Additionally, the reconstructed

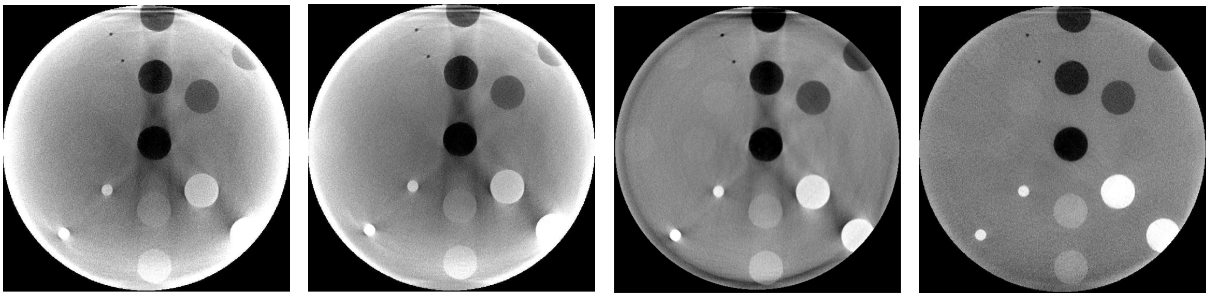

(a) Uncorrected. (b) Narrow scan. (c) Uniform scatter. (d) C-arm iPMSE.

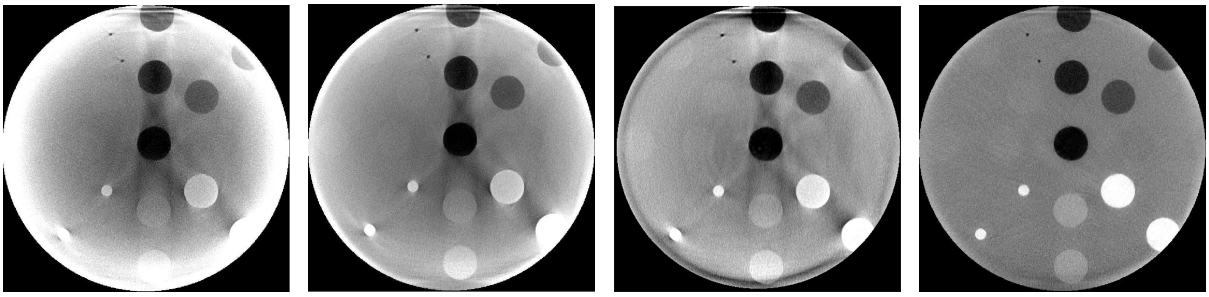

(e) Uncorrected. (f) Narrow scan. (g) Uniform scatter. (h) C-arm iPMSE.

FIG. 11. Reconstructed images of the acquisitions with the full Electron Density Phantom. In the first row, the antiscatter grid is used, in the second row, the antiscatter grid is removed from the system. The streak on top at the border of the FOV in each reconstruction results from the collimator edge, which slips into the FOV. Grayscale window: $C = 0$ HU, $W = 2000$ HU.

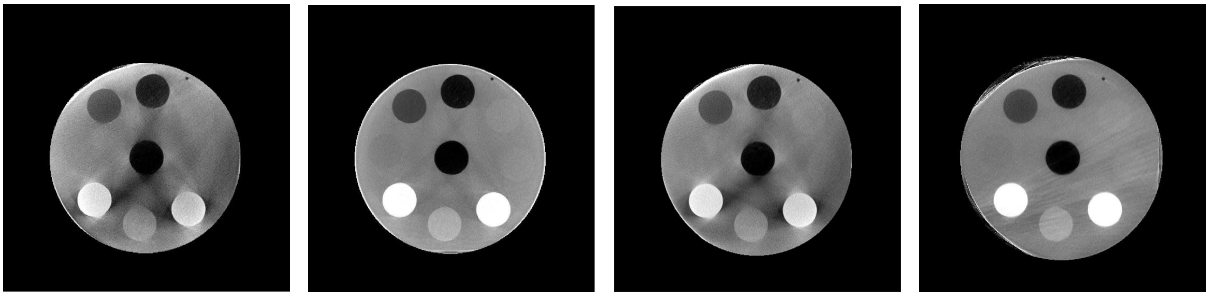

(a) Uncorrected. (b) Narrow scan. (c) Uniform scatter. (d) C-arm iPMSE.

FIG. 12. Reconstructed images of the acquisitions of the smaller, elliptical Electron Density Phantom. Grayscale window: $C = 0$ HU, $W = 2000$ HU.

FOV is larger compared to the narrow scan acquisition.

Currently, streaking artifacts appear in regions of dense material, which was visible in one of the phantom experiments. This is due to the photon starvation effect, which is amplified by the scatter correction when the estimated scatter signal is subtracted from

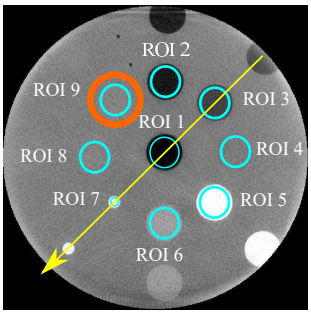

(a) ROIs in the big phantom.

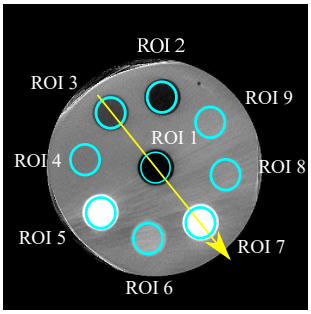

(b) ROIs in the small phantom.

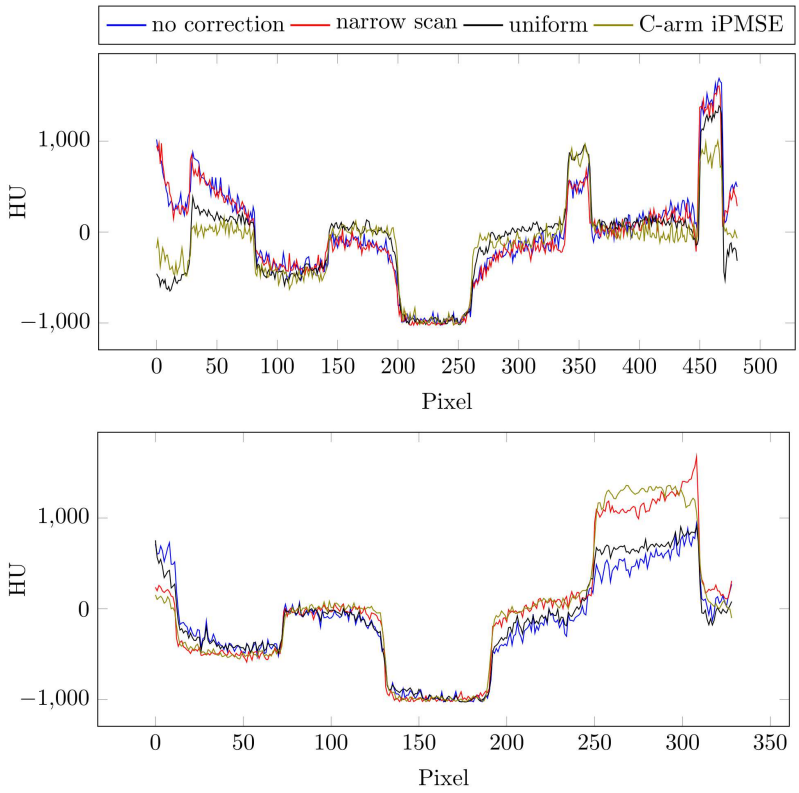

(c) Line profiles.

FIG. 13. ROIs and line profiles of the reconstructions with antiscatter grid. Top: full Electron Density Phantom. Bottom: inner ring Electron Density Phantom.

TABLE IV. Value of the MTF at 50% for each of the phantom experiments.

Experiment	Uncorrected	Narrow scan	Uniform Scatter	C-arm iPMSE
Big phantom with ASG	0.58	0.47	0.38	0.46
Big phantom without ASG	0.48	0.48	0.38	0.38
Small phantom with ASG	0.56	0.69	0.33	0.43

these regions. In our case, this effect appeared due to additional highly absorbing material, which was placed next to the phantom only for this scan in order to achieve an elliptic shape and a high tube current modulation. This behavior must be investigated in more detail.
330 The additional material next to the Electron Density Phantom further caused overexposure at the border of the phantom, which results from high exposure parameters due to the high attenuation of the material. Moreover, the combination of the *C-arm iPMSE* method

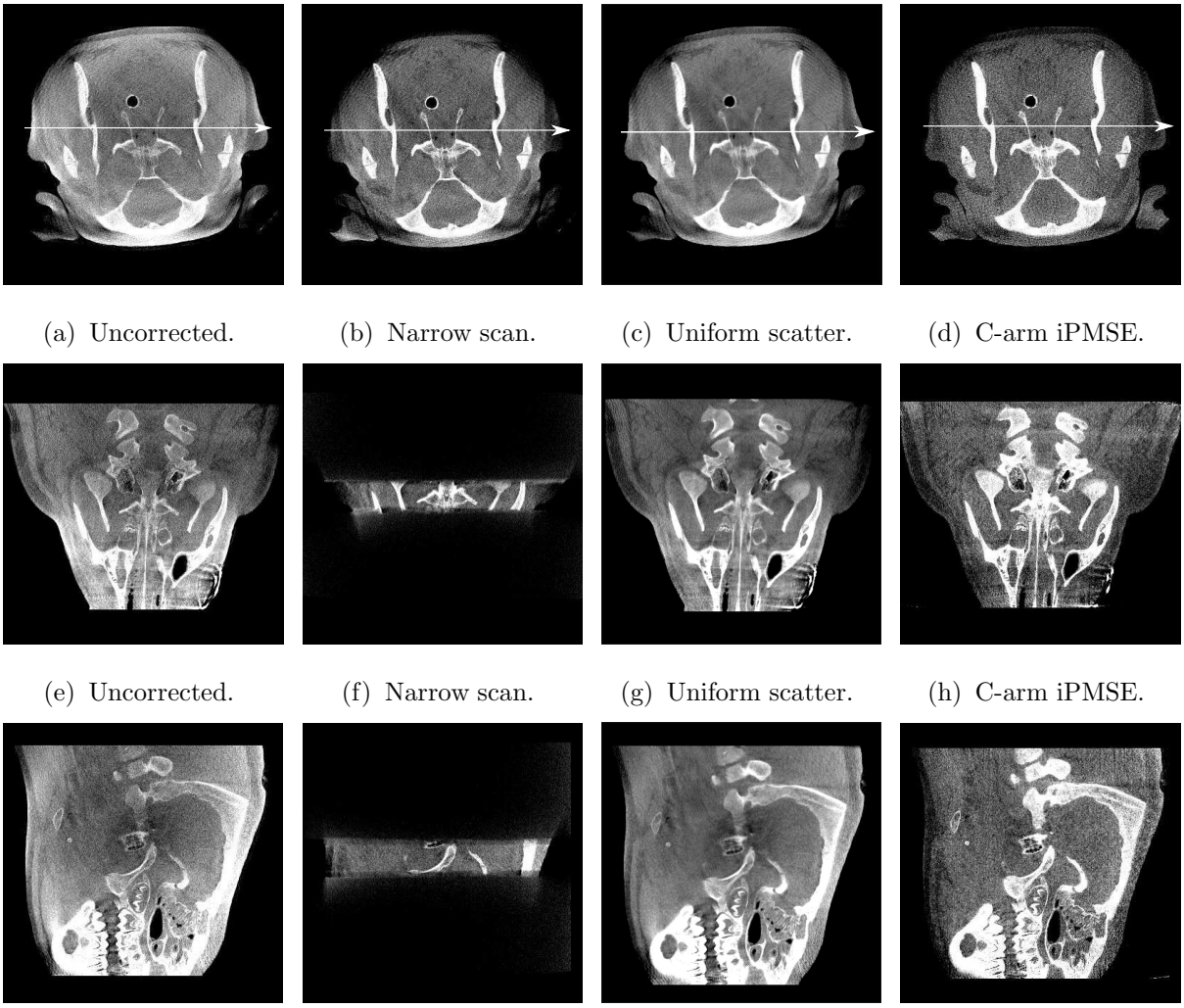

(a) Uncorrected. (b) Narrow scan. (c) Uniform scatter. (d) C-arm iPMSE.

(e) Uncorrected. (f) Narrow scan. (g) Uniform scatter. (h) C-arm iPMSE.

(i) Uncorrected. (j) Narrow scan. (k) Uniform scatter. (l) C-arm iPMSE.

FIG. 14. Reconstructed images of the pig head. Grayscale window: $C = 100$ HU, $W = 800$ HU. No antiscatter grid was used.

with the antiscatter grid was investigated, but its use proved to have little effect on the reconstruction results.

Some ring artifacts appeared in the *C-arm iPMSE* corrected images, which may have two underlying causes. On the one hand, the spectral properties of the X-rays introduce beam hardening. One solution would be to optimize the modulator material further, as done in [28] or to apply the method proposed in [29]. On the other hand, remnants of the modulator pattern could be also responsible for this artifact.

However, without a ground truth scatter estimate, it is difficult to show the detailed performance of the method. Also, overall evaluation is affected by the noise suppression,

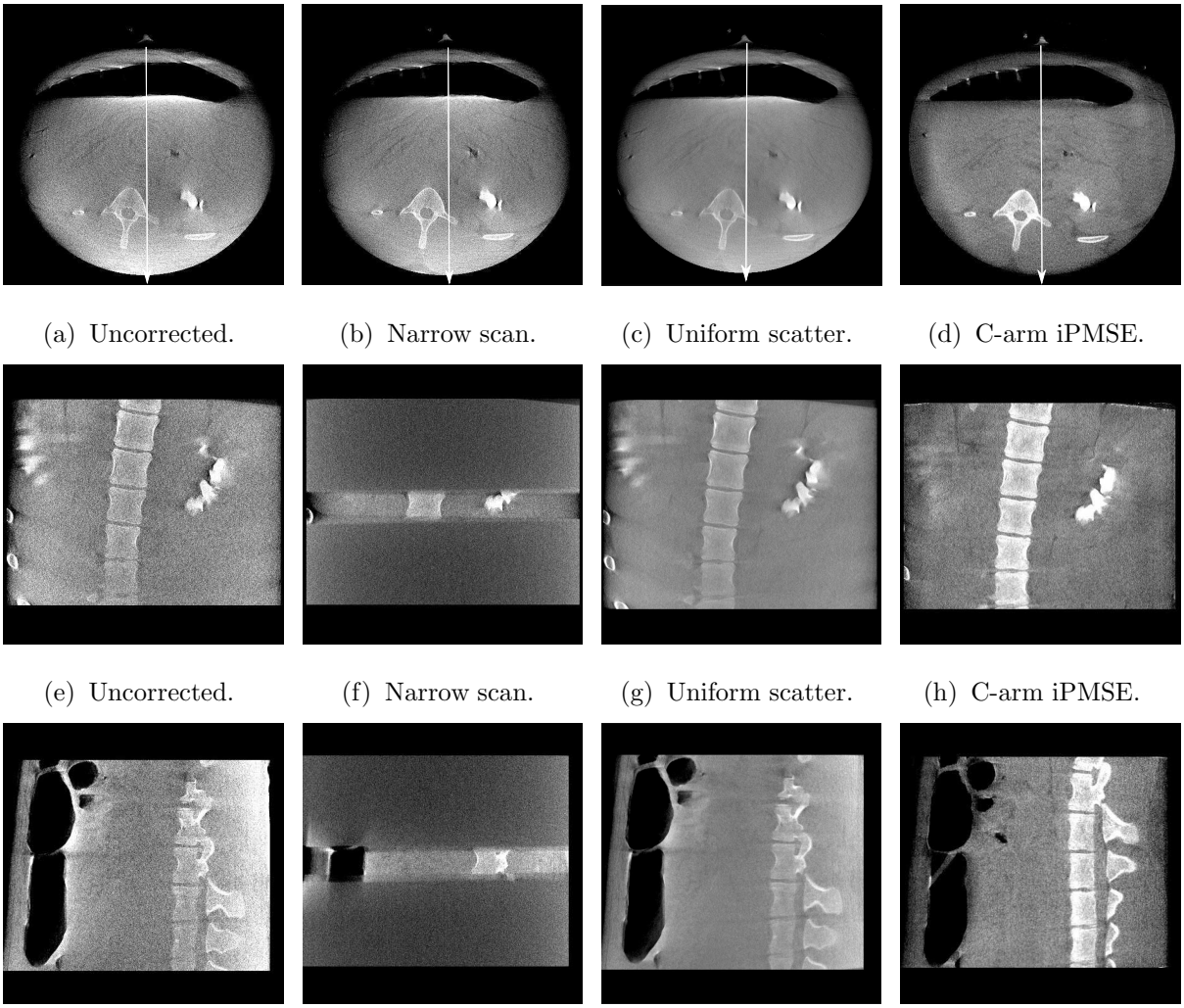

(a) Uncorrected. (b) Narrow scan. (c) Uniform scatter. (d) C-arm iPMSE.

(e) Uncorrected. (f) Narrow scan. (g) Uniform scatter. (h) C-arm iPMSE.

(i) Uncorrected. (j) Narrow scan. (k) Uniform scatter. (l) C-arm iPMSE.

FIG. 15. Reconstructed images of the pig abdomen. Grayscale window: $C = 0$ HU, $W = 1000$ HU. No antiscatter grid was used.

which is subsequent to the scatter correction [1]. Thus, not only the scatter correction itself is evaluated, but also the noise suppression. In general, a trade off of sharpness and contrast has to be found. One possibility is to do this task task-based [42] or to apply non-
345 linear filtering to smooth achieve a smoothed result while simultaneously preserve sharp edges [43, 44]. But this is not in the scope of this paper. Further, due to the experimental workflow of the in vivo scans, the table had to be moved to acquire the head and the abdomen of the pig with and without the modulator pattern mounted. Unfortunately, the table position could not be reproduced for both scans, which results in a slight shift of the
350 reconstruction and in the missing rip in the one reconstruction.

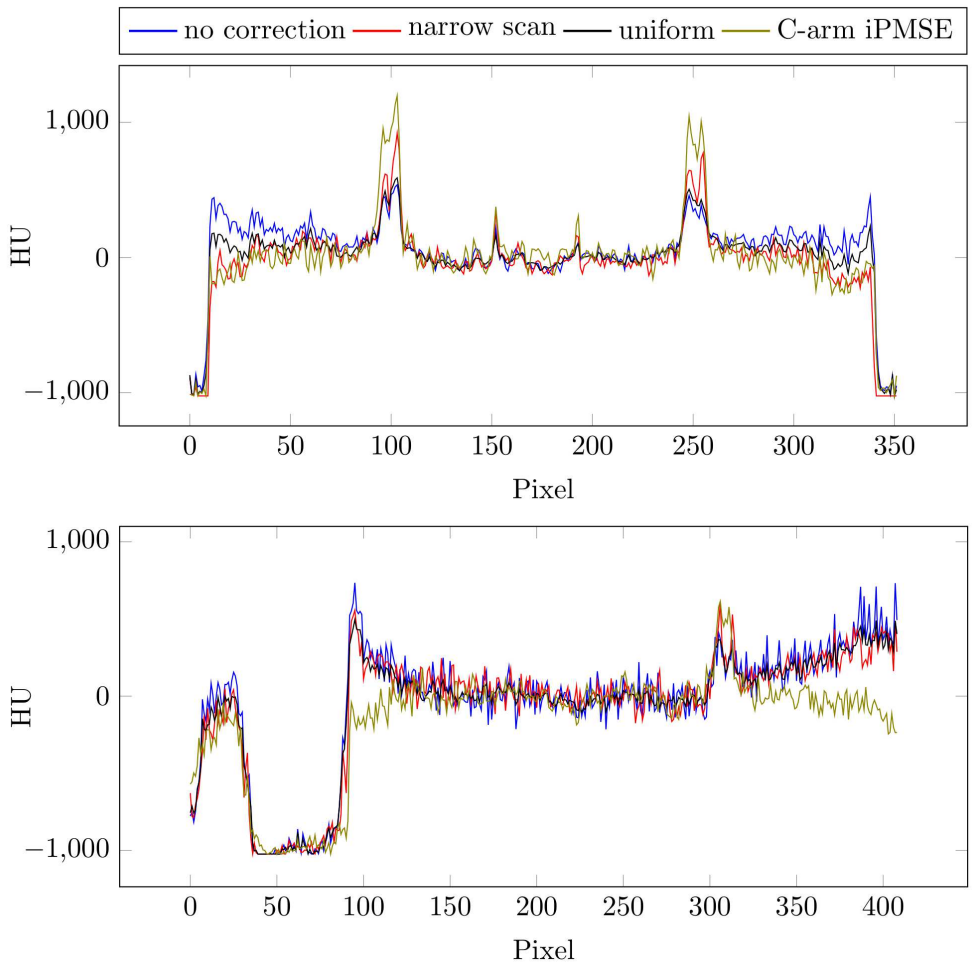

FIG. 16. Line profiles through the reconstructions of the in vivo head and the abdomen data. The locations of the lines are indicated in the axial images in Figure 14 and Figure 15, respectively.

The narrow scan is not sufficient as a reference for larger irradiated volumes since the narrowest collimation of approximately 20 mm in the isocenter is too wide and thus too much scatter remains in the projections.

V. CONCLUSION

We presented a new scatter correction method for a clinical C-arm CBCT by extending an existing method using a primary modulator. The occurring challenges on a clinical system are the C-arm motion and tube current modulation, which were overcome with establishing a modulator database, approximation of the amplitudes and a final registration step. We have shown that using a primary modulator for scatter correction on a clinical C-arm system

is possible. Image quality has been superior to the narrow scan and the uniform scatter corrected reconstructions, while being able to reconstruct the full FOV. Scatter artifacts could be well reduced in the reconstructions of phantom scans and in vivo data.

ACKNOWLEDGMENTS

The authors gratefully acknowledge funding support from the NIH Shared Instrument Grant S10 RR026714 supporting the zeego@StanfordLab, the NIH 1R21EB019597, the German Research Foundation (DFG), as part of the Research Training Group 1773 Heterogeneous Image Systems, and the DAAD. The authors thank Sanjit Datta and Waldo Hinshaw for supporting the experimental work.

CONFLICTS OF INTEREST

The authors Martin Berger, Kerstin Müller, Ludwig Ritschl, and Rebecca Fahrig are now with the Siemens Healthcare GmbH, Forchheim, Germany. During the work on this research topic, none of the above mentioned authors have been affiliated with Siemens. No funding from Siemens was received for this project.

---

[1] L. Zhu, J. Wang, and L. Xing, "Noise suppression in scatter correction for cone-beam CT," *Medical Physics*, vol. 36, no. 3, pp. 741–752, 2009.

[2] E.-P. Rührnschopf and K. Klingenbeck, "A general framework and review of scatter correction methods in x-ray cone-beam computerized tomography. Part 1: Scatter compensation approaches," *Medical Physics*, vol. 38, no. 7, pp. 4296–4311, 2011.

[3] J. H. Siewerdsen, D. J. Moseley, B. Bakhtiar, S. Richard, and D. A. Jaffray, "The influence of antiscatter grids on soft-tissue detectability in cone-beam computed tomography with flat-panel detectors," *Medical Physics*, vol. 31, no. 12, pp. 3506–3520, 2004.

[4] C. Luckner, A. Maier, and F. Dennerlein, "Schätzung von Faltungskernen für die Streusignalkorrektur in der Röntgenprojektionsradiographie aus mittels gewichteter Differenzen erzeugten Streustrahlbildern," in *Bildverarbeitung für die Medizin*. Springer, 2014, pp. 103–08.

[5] S. Hsieh, "Estimating scatter in cone beam CT with striped ratio grids: A preliminary investigation," *Medical Physics*, vol. 43, no. 9, pp. 5084–5092, 2016.

[6] J. A. Sorenson and J. Floch, "Scatter rejection by air gaps: an empirical model," *Medical Physics*, vol. 12, no. 3, pp. 308–316, 1985.

[7] L. Chen, C. C. Shaw, M. C. Altunbas, C.-J. Lai, X. Liu, T. Han, T. Wang, W. T. Yang, and G. J. Whitman, "Feasibility of volume-of-interest (VOI) scanning technique in cone beam breast CT-a preliminary study," *Medical Physics*, vol. 35, no. 8, pp. 3482–3490, 2008.

[8] E.-P. Rührnschopf and K. Klingenbeck, "A general framework and review of scatter correction methods in cone beam CT. Part 2: scatter estimation approaches," *Medical Physics*, vol. 38, no. 9, pp. 5186–5199, 2011.

[9] J. H. Siewerdsen, M. J. Daly, B. Bakhtiar, D. J. Moseley, S. Richard, H. Keller, and D. A. Jaffray, "A simple, direct method for x-ray scatter estimation and correction in digital radiography and cone-beam CT," *Medical Physics*, vol. 33, no. 1, pp. 187–197, 2006.

[10] R. Ning, X. Tang, and D. Conover, "X-ray scatter correction algorithm for cone beam CT imaging," *Medical Physics*, vol. 31, no. 5, pp. 1195–1202, 2004.

[11] L. Ouyang, K. Song, and J. Wang, "A moving blocker system for cone-beam computed tomography scatter correction." *Med Phys*, vol. 40, no. 7, p. 71903, 2013.

[12] X. Chen, L. Ouyang, H. Yan, X. Jia, B. Li, Q. Lyu, Y. Zhang, and J. Wang, "Optimization of the geometry and speed of a moving blocker system for cone-beam computed tomography scatter correction," in *Proc. 4th Intl. Mtg. on image formation in X-ray CT*, 2016, pp. 553–556.

[13] T. Niu and L. Zhu, "Scatter correction for full-fan volumetric CT using a stationary beam blocker in a single full scan," *Medical Physics*, vol. 38, no. 11, p. 6027, 2011.

[14] M. Zellerhoff, B. Scholz, E.-P. Rührnschopf, and T. Brunner, "Low contrast 3D-reconstruction from C-arm data," *Proceedings of SPIE*, vol. 5745, pp. 646–655, 2005.

[15] B. Bier, A. Maier, H. G. Hofmann, C. Schwemmer, Y. Xia, T. Struffert, and J. Hornegger, "Convolution-Based Truncation Correction for C-Arm CT using Scattered Radiation," in *Bildverarbeitung für die Medizin*. Springer, 2013, pp. 338–343.

[16] L. Shi, S. Vedantham, A. Karellas, and L. Zhu, "Library based x-ray scatter correction for dedicated cone beam breast CT," *Medical Physics*, vol. 43, no. 8, pp. 4529–4544, 2016.

[17] G. J. Bootsma, F. Verhaegen, and D. A. Jaffray, "Efficient scatter distribution estimation and correction in CBCT using concurrent Monte Carlo fitting," *Medical Physics*, vol. 42, no. 1, pp. 54–68, 2015.

[18] G. Jarry, S. a. Graham, D. J. Moseley, D. J. Jaffray, J. H. Siewerdsen, and F. Verhaegen, "Characterization of scattered radiation in kV CBCT images using Monte Carlo simulations," *Medical Physics*, vol. 33, no. 11, pp. 4320–4329, 2006.

[19] W. Swindell and P. M. Evans, "Scattered radiation in portal images: a Monte Carlo simulation and a simple physical model." *Medical Physics*, vol. 23, no. 1, pp. 63–73, 1996.

[20] A. Bani-Hashemi, E. Blanz, J. Maltz, D. Hristov, and M. Svatos, "Cone Beam X-Ray Scatter Removal Via Image Frequency Modulation and Filtering," *Medical Physics*, vol. 32, no. 6, p. 2093, 2005.

[21] L. Zhu, N. R. Benett, and R. Fahrig, "Scatter correction method for x-ray CT using primary modulation: Theory and preliminary results," *IEEE Transactions on Medical Imaging*, vol. 25, no. 12, pp. 1573–1587, 2006.

[22] L. Zhu, "Local filtration based scatter correction for cone-beam CT using primary modulation," *Medical Physics*, vol. 43, no. 11, pp. 6199–6209, 2016.

[23] L. Zhu, J. StarLack, N. R. Bennett, T. Li, L. Xing, and R. Fahrig, "Improved Scatter Correction for X-ray Conebeam CT Using Primary Modulation," *Proc. of SPIE*, vol. 6510, pp. 65 101U–65 101U–8, 2007.

[24] L. Zhu, R. Bennett, and R. Fahrig, "Scatter Correction for X-ray Imaging Using Primary Modulation: A Phantom Study for CBCT," *IFMBE Proceedings*, vol. 14, pp. 1372–1375, 2009.

[25] H. Gao, L. Zhu, and R. Fahrig, "Optimization of System Parameters for Modulator Design in X-ray Scatter Correction Using Primary Modulation," in *Proc. of SPIE*, vol. 7622, no. 8, 2010, p. 76222A.

[26] H. Gao, R. Fahrig, N. R. Bennett, M. Sun, J. Star-Lack, and L. Zhu, "Scatter correction method for x-ray CT using primary modulation: Phantom studies," *Medical Physics*, vol. 37, no. 2, pp. 934–946, 2010.

[27] H. Gao, T. Niu, L. Zhu, and R. Fahrig, "Evaluation of an erbium modulator in x-ray scatter correction using primary modulation," in *Proc. SPIE*, vol. 7961, 2011, p. 796122.

[28] H. Gao, L. Zhu, and R. Fahrig, "Modulator design for x-ray scatter correction using primary modulation: material selection." *Medical Physics*, vol. 37, no. 8, pp. 4029–37, 2010.

[29] R. Grimmer, R. Fahrig, W. Hinshaw, H. Gao, and M. Kachelrieß, "Empirical cupping correction for CT scanners with primary modulation (ECCP)," *Medical Physics*, vol. 39, no. 2, pp. 825–831, 2012.

[30] K. Schörner, M. Goldammer, K. Stierstorfer, J. Stephan, and P. Böni, "Scatter correction method by temporal primary modulation in X-ray CT," *IEEE Transactions on Nuclear Science*, vol. 59, no. 6, pp. 3278–3285, 2012.

[31] Á. Horváth, D. Hadházi, and G. Horváth, "Analysis of primary modulation based x-ray scatter correction methods," *Medical Physics*, vol. 43, no. 11, pp. 5794–5807, 2016.

[32] L. Ritschl, R. Fahrig, M. Knaup, J. Maier, and M. Kachelrieß, "Robust primary modulation-based scatter estimation for cone-beam CT," *Medical Physics*, vol. 42, no. 1, p. 469, 2015.

[33] B. Bier, K. Müller, M. Berger, J.-H. Choi, L. Ritschl, M. Kachelrieß, R. Fahrig, and A. Maier, "Scatter Correction for C-Arm CT Using Primary Modulation," in *The 4th International Conference on Image Formation in X-ray Computed Tomography*, 2016, pp. 383–386.

[34] S. Ourselin, A. Roche, S. Prima, and N. Ayache, "Block matching: A general framework to improve robustness of rigid registration of medical images," *MICCAI*, vol. 1935, pp. 557–566, 2000.

[35] A. Maier, H. G. Hofmann, M. Berger, P. Fischer, C. Schwemmer, H. Wu, K. Müller, J. Hornegger, J.-H. Choi, C. Riess, A. Keil, and R. Fahrig, "CONRAD - A software framework for cone-beam imaging in radiology," *Medical Physics*, vol. 40, no. 11, p. 111914, 2013.

[36] C. Schmidgunst, D. Ritter, and E. Lang, "Calibration model of a dual gain flat panel detector for 2D and 3D x-ray imaging." *Medical Physics*, vol. 34, no. 9, pp. 3649–3664, 2007.

[37] A. Maier, L. Wigstrom, H. G. Hofmann, J. Hornegger, L. Zhu, N. Strobel, and R. Fahrig, "Three-dimensional anisotropic adaptive filtering of projection data for noise reduction in cone beam CT." *Medical Physics*, vol. 38, no. 11, pp. 5896–5909, 2011.

[38] J. Hornegger, A. Maier, and M. Kowarschik, "CT Image Reconstruction Basics" *MR and CT Perfusion and Pharmacokinetic Imaging: Clinical Applications and Theoretical Principles*, Wolters Kluwers, 2016.

[39] D. Prell, Y. Kyriakou, and W. A. Kalender, "Comparison of ring artifact correction methods for flat-detector CT." *Physics in Medicine and Biology*, vol. 54, no. 12, pp. 3881–95, 2009.

[40] I. Sabo-Napadensky and O. Amir, "Reduction of Scattering Artifact in Multislice CT," *Proceedings of SPIE*, vol. 5745, pp. 983–991, 2005.

[41] R. L. Baer, "The Circular Edge Spatial Frequency Response Test," in *Proceedings of SPIE*, vol. 5294, 2003, pp. 71–81.

[42] H. Dang, J. W. Stayman, J. Xu, A. Sisniega, W. Zbijewski, X. Wang, D. H. Foos, N. Aygun, V. E. Koliatsos, and J. H. Siewerdsen, "Task-based regularization design for detection of intracranial hemorrhage in cone-beam CT," in *Proc. 4th Intl. Mtg. on image formation in X-ray CT*, 2016, pp. 537–560.

[43] A. Maier, L. Wigstrom, H. G. Hofmann, J. Hornegger, L. Zhu, N. Strobel, and R. Fahrig, "Three-dimensional anisotropic adaptive filtering of projection data for noise reduction in cone beam CT." *Medical Physics Phys*, vol. 38, no. 11, pp. 5896–5909, 2011.

[44] A. Maier and R. Fahrig, "Graphics Processing Unit-Based High Performance Computing in Radiation Therapy" *GPU Denoising for Computed Tomography*, 1st ed., Xun Jia and Jiang Steve, 2015.